




Compact mid-infrared dual-comb spectrometer for outdoor spectroscopy

GABRIEL YCAS,^{1,2} FABRIZIO R. GIORGETTA,^{1,2}  JACOB T. FRIEDLEIN,² DANIEL HERMAN,^{1,2} KEVIN C. COSSEL,² ESTHER BAUMANN,^{1,2} NATHAN R. NEWBURY,² AND IAN CODDINGTON^{2,*}

¹Department of Physics, University of Colorado at Boulder, 390 UCB, Boulder CO 80309-0390, USA

²Applied Physics Division, National Institute for Standards and Technology, 325 Broadway, Boulder CO 80305, USA

*ian.coddington@nist.gov

Abstract: This manuscript describes the design of a robust, mid-infrared dual-comb spectrometer operating in the 3.1- μm to 4- μm spectral window for future field applications. The design represents an improvement in system size, power consumption, and robustness relative to previous work while also providing a high spectral signal-to-noise ratio. We demonstrate a system quality factor of 2×10^6 and 30 hours of continuous operation over a 120-meter outdoor air path.

1. Introduction

Dual-comb spectroscopy (DCS) using mode-locked lasers provides an unparalleled combination of broad spectral bandwidth, high resolution, high signal-to-noise ratio, and high frequency accuracy [1–14]. In the near-IR, fielded open-path dual-comb spectrometers [15] based on robust polarization maintaining (PM) Er: fiber frequency combs have been used for open-path greenhouse gas monitoring [16–18], leak detection in oil and gas infrastructure [19,20], combustion monitoring [21,22], and materials characterization [23,24], often exceeding the capabilities of conventional spectrometers. Extending the wavelength coverage of frequency combs to the mid-IR allows access to strong, fundamental, ro-vibrational molecular bands and greatly enhances sensitivity [25]: demonstrations of microscopy [26], open-path detection of volatile organic chemicals [8,27,28], studying combustion dynamics [29,30], detection of radicals [31,32], and bio monitoring [33,34] suggest an array of possible directions for this technology. If these laboratory mid-IR DCS systems could be made fieldable in the same manner as the near-IR systems, it would enable new measurement capabilities. While some DCS applications could certainly be addressed with compact, portable and increasingly advanced quantum-cascade-frequency combs [30,33,35–42], inter-band cascade frequency combs [43], and mid-IR electro-optic combs [44,45], certain applications, such as atmospheric monitoring, require a combination of broad spectral bandwidth and high resolution that is currently not available with QCL-based DCS.

Here we demonstrate a fieldable mid-IR dual-comb spectrometer based on PM Er: fiber frequency combs and difference-frequency generation (DFG) [2,8,12–14,26,27,46,47]. Similar intra-cavity DFG [48] and optical parametric oscillator [11,49–52] techniques are increasing in sophistication, but we feel that two-branch DFG is currently the optimal way to construct a robust, modelocked-laser-based, mid-IR dual-comb spectrometer for field applications because of the simple, single pass frequency conversion from near-IR to mid-IR. Unlike our previous systems [12], this new approach does not require Yb: fiber amplifiers and large grating compressors/stretchers, which results in greatly decreased size, cost, and complexity and thus significantly improved reliability compared to previous systems. We show that this system provides up to 6 mW of light spanning the 3–4 μm atmospheric transparency window. The near-term goal of this work is to build on previous near-IR DCS for studying emissions from oil and gas infrastructure with the goal of being able to directly measure the volatile organic chemicals that impact local air quality. With this in mind we demonstrate the capability of the system over a 120-m outdoor open-path

measurement spanning 30 continuous hours with 100% instrument up-time. This demonstrates the stability of the new DCS system and shows its potential for atmospheric monitoring outside of the laboratory.

2. Robust mid-IR comb design

The basic mid-IR comb design is shown in Figs. 1(a) and 1(b) and is based on a PM mode-locked Er: fiber laser [53] with a 200-MHz repetition rate. The output from the near-IR oscillator is split into one branch for laser stabilization and a second branch for mid-IR light generation via DFG. This second branch is preamplified to ~ 50 mW in a 50 cm long, normal-dispersion, singly-pumped erbium-doped fiber amplifier (EDFA) before being, again, split into two branches to provide signal and pump light at $1.1 \mu\text{m}$ and $1.56 \mu\text{m}$ respectively. The signal branch consists of an EDFA and a nonlinear optical fiber optimized to generate ~ 40 mW of light between $1.04 \mu\text{m}$ and $1.12 \mu\text{m}$. The EDFA uses ~ 170 cm of normal-dispersion PM Er: fiber and is triply pumped with 900 mW, 976 nm laser diodes (one forward, two reverse) to produce an average power of ~ 400 mW with a pulse duration of ~ 65 fs. The pulse is then spectrally broadened in ~ 20 cm of polarization-maintaining (PM) highly-nonlinear optical fiber (HNLF) with a nominal dispersion of 2.2 ps/nm/km at 1550 nm. The $1.1 \mu\text{m}$ pulses are ~ 800 fs in length. The light for the pump branch is amplified in 100 cm of anomalous-dispersion PM Er: fiber that is reverse pumped with a single 900 mW, 976 nm laser diode. To reduce the system sensitivity to small timing drifts, the $1.56 \mu\text{m}$ light is stretched in 5 m of PM1550 fiber before it is amplified by the EDFA. The result is an average power of ~ 175 mW and a pulse duration of ~ 1 ps.

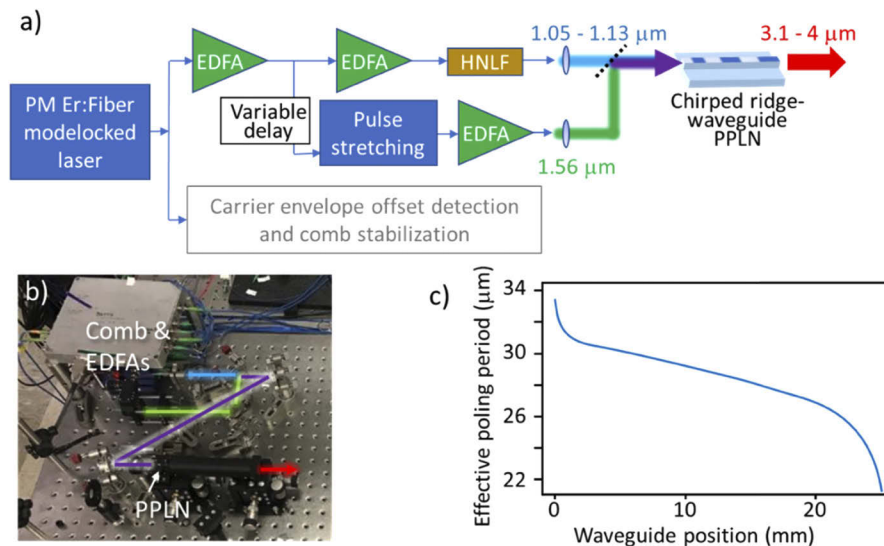


Fig. 1. System diagram for a single comb showing (a) a block diagram of a single mid-IR frequency comb, (b) a photograph of the system in (a) with beam paths added, and (c) the chirped waveguide PPLN poling design. PM: polarization maintaining, EDFA: erbium doped fiber amplifier, HNLF: highly-nonlinear fiber, PPLN: periodically poled lithium niobate.

The broadband signal light is collimated into free-space with an off-axis parabolic mirror (OAP) of focal length $f = 15$ mm while the narrowband pump light is collimated into free-space with a $f = 18.36$ mm triplet lens. To generate the mid-IR light, the pump and signal pulses are combined on a dichroic beam splitter and coupled into a periodically-poled lithium niobate (PPLN) waveguide using an $f = 15$ mm OAP with about 65% efficiency. The waveguide is a 15

$\mu\text{m} \times 16 \mu\text{m}$ ridge waveguide whose chirped poling design is shown in Fig. 1(c). The pump and signal pulses are temporally overlapped in the waveguide by tuning a variable path length section of the $1.56 \mu\text{m}$ pump branch, resulting in up to 6 mW of mid-IR light in a spectrum simultaneously spanning from $3.1 \mu\text{m}$ to $4 \mu\text{m}$. Due to the long temporal duration of the $1.56 \mu\text{m}$ pulses (~ 1 ps), the shape of this spectrum depends only weakly on the relative pulse delay between the two branches, providing a high level of long-term stability. Finally, mid-IR light exiting the waveguide is collimated using a $f = 5.95$ mm aspheric lens.

Although the signal power at $1.1 \mu\text{m}$ is significantly lower here than in the previous work [12], the use of waveguide PPLN enables the generation of milliwatt level mid-IR light. This high conversion efficiency can be explained by the Landau-Zener theory for adiabatic rapid passage as applied to non-linear frequency conversion [54,55]. The theoretical efficiency of frequency conversion, η_{LZ} , in the adiabatic regime (assuming a strong, time-invariant, and undepleted pump field) is a function of pump intensity, I_P , and is given by

$$\eta_{LZ} = [1 - \exp(-BI_P)] \quad (1)$$

where B is a negative number that can be calculated from the waveguide material properties and geometry as shown in refs. [54,55]. The efficiency of our conversion can also be estimated by fitting the data in Fig. 2(d) to the form $I_{\text{Mid-IR}} = [1 - \exp(-BI_P)]A$ and estimating the asymptote of

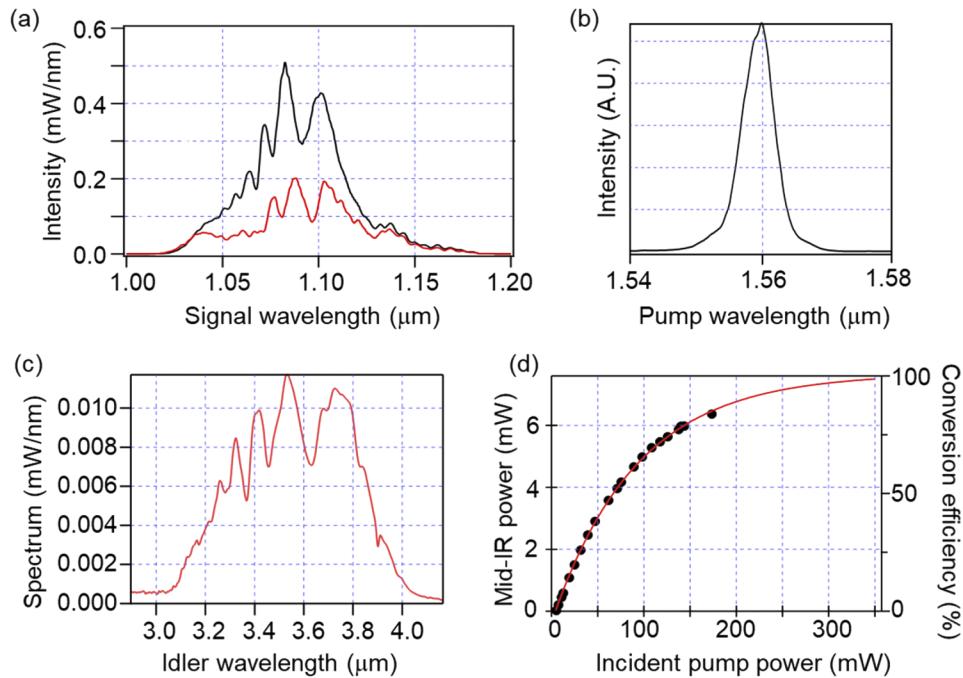


Fig. 2. (a) Spectrum of the $1.1 \mu\text{m}$ signal light measured after the waveguide shown both without pump-signal pulse overlap (black) and with overlap (red). The difference shows depletion of the signal light in the converted band. In this case, incident pump power was ~ 70 mW corresponding to $\sim 50\%$ conversion of the $1.1 \mu\text{m}$ light. (b) Spectrum of the pump pulse. (c) Spectrum of the generated mid-IR comb idler light from a single comb. (d) Measured mid-IR output power as function of the incident $1.56 \mu\text{m}$ power (black points) and a fit to the Landau-Zener approximation (red line). At the higher input power levels, there is clear evidence of saturation in the mid-IR output. The fit asymptotically approaches 7.6 mW. The $1.1 \mu\text{m}$ light is held at a fixed power throughout.

the function as 100% conversion of the phase matched 1 μm light. Figure 2(d) shows the fit of our experimental results to Eq. (1) in red. This fit yields $A = 7.5$ mW, implying an 85% conversion efficiency at our peak, 175 mW, incident pump power, and $B = -3.5$ cm^2/GW , which is within 20% of the calculated value $B = -3$ cm^2/GW , suggesting that the system is well described by the adiabatic rapid passage model.

3. Establishing mutual coherence for high SNR dual-comb operation

In DCS, high mutual coherence between the combs is required for both high resolution and high signal-to-noise (SNR) operation [1]. Here we enforce this coherence with a combination of both active phase locking and digital correction of the interferogram signal. The active phase locking part of the frequency control scheme is shown in Fig. 3. In this control scheme the comb stability and the frequency accuracy of the recorded spectra are derived from a 10 MHz quartz oscillator that is used to lock both the repetition rate of the “master” comb (comb 1) and the carrier envelope-offset frequencies, $f_{ceo,1(2)}$, of combs 1 and 2. To complete the stabilization of both degrees of freedom of the combs we establish optical coherence by locking a single tooth from the second comb (comb 2) to a cw external cavity diode laser (ECDL), which is in turn locked to a tooth of comb 1. This approach has two significant advantages for portability over our previous mid-IR DCS system [12]. First, our previous work relied on a laboratory-bound, cavity-stabilized fiber laser to provide the mutual coherence and frequency accuracy. Replacing this with the simpler and more compact quartz oscillator and ECDL was critical for field reliability. Secondly, our previous approaches relied on high bandwidth (~ 100 kHz), low phase noise (< 1 radian) locks between the combs and the cw laser. Here we used only low-bandwidth piezoelectric actuators (~ 1 kHz) and temperature tuning to servo the comb cavity length and lock the comb to the cw laser. This loose locking scheme is simpler and robust, but it can also leave >20 radians of residual optical phase noise between the two combs even over the short duration of a single interferogram acquisition. If not removed, this residual noise will cripple the system’s frequency resolution and ability to coherently average.

To compensate for this higher level of phase noise, interferogram acquisition and co-adding is performed using an improved version of the field-programmable gate array (FPGA)-based acquisition system initially demonstrated at the Université Laval and described in Refs. [4–6,12]. The FPGA uses the residual phase noise from the four comb locks to calculate and perform a real-time, sample-by-sample, phase and timing correction to each point of the interferogram to compensate for high frequency laser noise. The FPGA then performs a second global phase correction to each interferogram to correct out-of-loop timing shifts, and finally co-adds sequential interferograms for long-term averaging. Point-by-point interferogram corrections are, at this point, well established using both digital and analog approaches [4–6,10,12,14,38,41,56–58] and the mathematical framework of our FPGA-based approach is thoroughly described in refs. [5,12]. The frequency accuracy of the spectrum is still set by the 10 MHz input reference signal through the comb stabilization.

However, the resampling required by the point-by-point timing correction poses a challenge at such high phase noises. Previous versions of this algorithm employed a linear interpolation between samples, which is more straightforward to implement in firmware but creates spurious effects for large timing errors, particularly for interferogram frequency components approaching the Nyquist sampling frequency. In this work, the real-time interpolation implemented on the FPGA was upgraded from a linear interpolation to a 50-point sinc function (quasi-band limited interpolation) [59]. Although technically more challenging, the entire algorithm could be implemented on a Xilinx Virtex-7 VX485T. It enables both accurate interpolation at radio frequencies up to $\sim 90\%$ of the Nyquist frequency and full real-time correction of time and phase in the presence of >100 fs of pulse timing jitter between combs.

To demonstrate the signal processing system's ability to remove large amounts of phase noise, we acquired 1.3-second-long time-series with and without the real-time corrections enabled for the locking conditions shown in Fig. 3(b). With corrections enabled, Figs. 4(a)–4(c), the individual centerbursts appear nearly identical and the Fourier transform of the complete time series reveals resolved comb teeth. Without any correction, Figs. 4(d)–4(f), the time-domain interferograms appear incoherent, and the spectra reflect this, with no resolved comb modes.

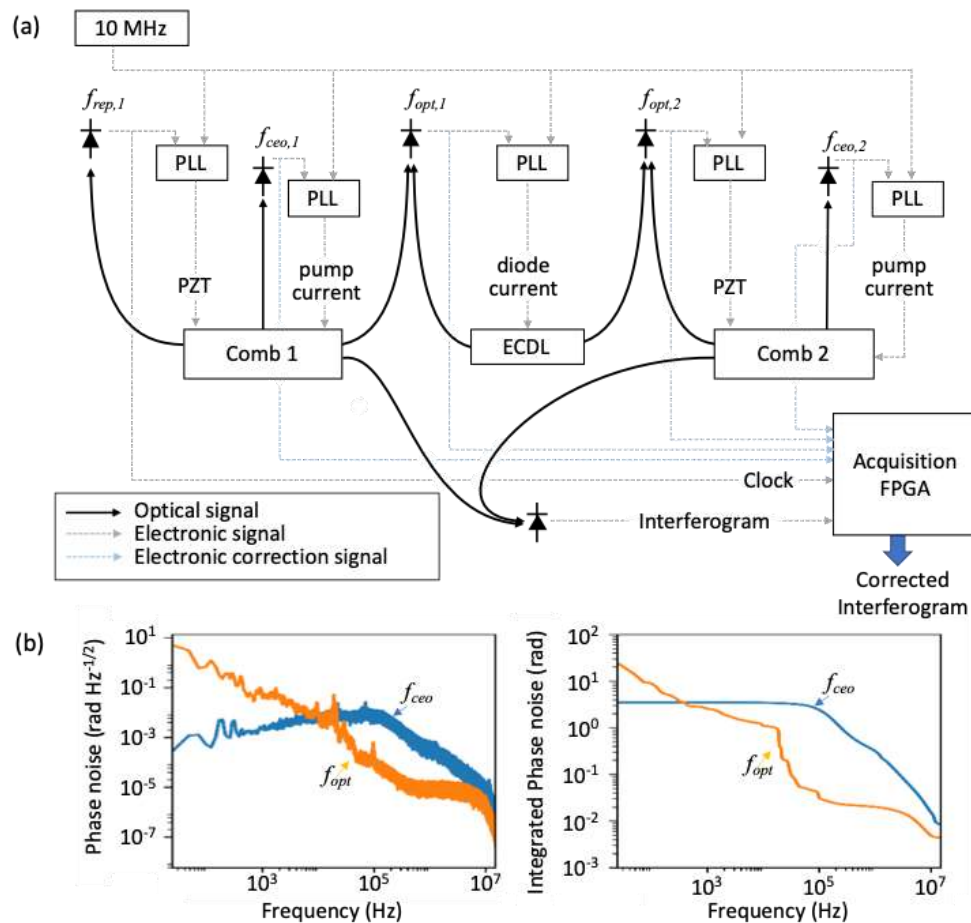


Fig. 3. Schematic of comb locking scheme. Frequency control flows roughly left to right. The repetition rate of the system is defined by a phase lock of the comb 1 repetition rate to a 10 MHz time base. Mutual coherence between the combs is established by locking both f_{ceo} frequencies and by offset locking of an external cavity diode laser (ECDL) to comb 1 ($f_{opt,1}$) and then locking comb 2 to the ECDL ($f_{opt,2}$). PLL: phase-locked loop. (b) Power spectral density (left) and integrated phase noise (right) for the differential phase noise between combs at the f_{ceo} and f_{opt} lock points.

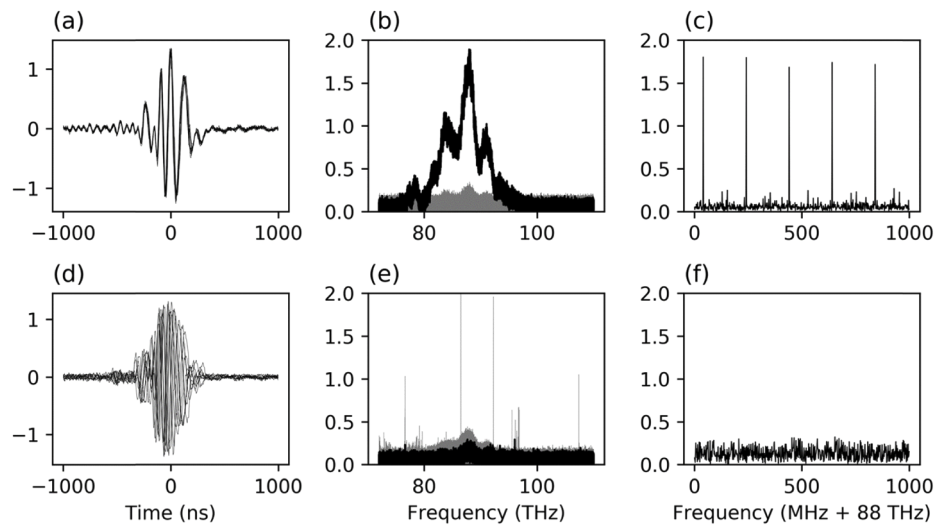


Fig. 4. (a) Ten sequential phase-corrected interferogram centerbursts overplotted on each other. (b) Scatter plot of the Fourier transform of a time series with 139 interferograms. Comb tooth peaks are plotted in black and the rest of the points are plotted gray. (c) Line plot of a zoom-in of (b) near center showing well resolved comb lines. (d-f) As above, but with no phase correction.

4. Outdoor DCS and continuous unattended operation

In addition to being able to operate with higher levels of phase noise, the new design reduces the susceptibility to thermal drift. In our previous mid-IR DFG sources, spectral stability has been limited by temporal walk-off between pump and signal pulses, or by misalignment [12]. The system described here is more stable because it does not require pulse stretchers/compressors or high-power Yb: fiber amplifiers. Moreover, the pump pulses in the new system are temporally stretched, reducing the likelihood of walk-off between the pump and signal pulses. These improvements allow the new mid-IR combs to operate unattended for days and provide more stable spectra, which translates into better sensitivity to broad absorbers.

The setup for outdoor dual-comb measurements over a 120-m path is shown in Fig. 5. First, the output of each mid-IR comb is combined on a 50:50 beamsplitter. One output port is coupled into a PM, single-mode, zirconium fluoride (ZrF_4) fiber with up to 60% efficiency using an $f = 7$ mm OAP and sent to a telescope platform. The PM fiber and polarizers in the telescope constrain the polarization of the launched light. This reduces structure in the baseline spectrum due to the interplay of a spectrally dependent launch polarization, pointing dependent polarization rotation on the corner cube, and polarization dependence of the beam splitter. Removing these polarization-dependent effects leads to a $>10x$ improvement in our ability to limit baseline structure on the recorded spectrum. Signal and reference interferograms are recorded on HgCdTe detectors mounted on the telescope. Both detectors are 200-MHz bandwidth, thermoelectrically cooled devices with an NEP of $15 \text{ pW/Hz}^{1/2}$.

Combining both beams before launching over the open path is, at this point, a very established technique for sensing for three reasons [1]. First, it suppresses relative path induced phase fluctuations between the two combs, which can degrade the SNR particularly in long open paths. Second, the co-linear approach allows the combs to be transmitted to the launch telescope in a single fiber, which greatly simplifies the optical design. Finally, while one sacrifices the benefit of a local oscillator for heterodyne gain, the overlapped spatial mode of the two combs ensures the beam scintillation will not degrade heterodyne efficiency.

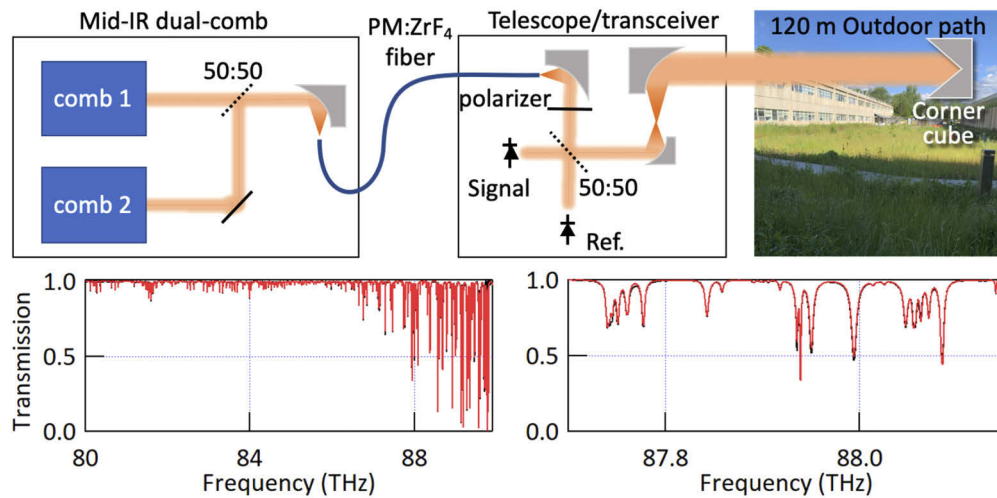


Fig. 5. Schematic of open-path dual-comb spectrometer. Mid-infrared light from two combs are combined and launched into a polarization-maintaining ZrF₄ fiber. The fiber transports light to the telescope system, which uses a reflective collimator and reflective beam expander to launch a collimated beam. At the end of the 120 m outdoor path a 5-inch-diameter corner-cube retro-reflector returns the light to the telescope. A linear polarizer in combination with the PM ZrF₄ fiber suppresses both temporal and spectral variation due to the input polarization. The bottom panels show a measured transmission spectrum averaged for 168 minutes achieved by dividing the signal spectrum with the reference spectrum and applying a piecewise polynomial baseline correction as discussed in ref [16] (black traces). The red traces are a model transmission using Hitran 2008 lineshape parameters for H₂O and CH₄ [60] and show good agreement with the measurement.

Figure 5 shows the measured open-path spectra processed in the traditional way using a piecewise polynomial baseline correction (see ref [16] for example). However, a goal of this system is to see larger molecules with broad absorption features that would also be removed by this baseline fit. Thus it is also useful to remove baseline structure in the measured spectra through a four-point normalization of the spectrum which preserves these features as outlined in Refs. [12,28]. The normalized spectra is calculated as follows

$$I_{norm}(\nu) = \frac{I_{Signal}/I_{Ref}}{I_{Signal,0}/I_{Ref,0}},$$

where I_{Signal} and I_{Ref} are the spectra recorded from the signal and reference detectors and $I_{Signal,0}$ and $I_{Ref,0}$ are the same signals recorded at a time zero when the chemical species of interest is not present. Using HITRAN 2016 [60] as a model we also fit and remove the absorption spectra of common small molecules, such as water and methane, from I_{Signal} and $I_{Signal,0}$ before normalization. Figure 6 shows an example of signal and reference spectra and the associated normalized spectra over several hours. Because of the system's stability, the spectral baseline remains flat ($\pm 2\%$) even when I_{Signal} and I_{Ref} are separated from $I_{Signal,0}$ and $I_{Ref,0}$ by intervals (Δt) of as much as 30 hours. The strongest impact on the spectral baseline is the water absorption features around 90 THz. Background comb structure, detector response and etalons visible in Fig. 6(a) can be strongly suppressed by the four-point normalization.

The improved baseline removal due to better system stability enhances our sensitivity to ambient ethane and propane over the outdoor path. Ethane and propane originate primarily from oil and gas production, and the Denver-Julesburg Basin – an active oil and gas extraction basin –

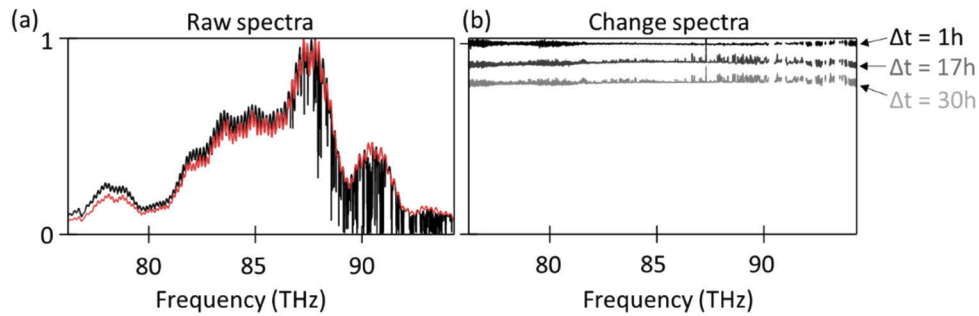


Fig. 6. (a) The raw reference spectrum (red) and signal spectrum (black) as acquired across a 120 m open-air path. Discrepancies between the reference and signal spectra are stable over time and can be removed by four-point normalization. (b) Comparison of normalized spectra for different delays across more than a day (offset for clarity), the variations are below $\pm 2\%$ as shown in the right panel. A linear baseline was removed from the change spectra. The structure at frequencies above 86 THz is due to changing water concentrations of the outdoor air. Traces are offset for clarity.

lies to the north-east of Boulder, which leads to wind direction-dependent ambient ethane and propane concentrations in the city. After fitting H_2O and CH_4 concentrations and removing their spectral signature, ethane and propane can be clearly seen in a 1-hour averaged spectrum taken during an easterly wind (Fig. 7). To determine concentrations, we fit with a model consisting of a cubic polynomial baseline and ethane and propane spectra [61], which yields a path averaged ethane concentration of 59 ppb (14.2 ppm·m) and propane concentration of 78 ppb (18.8 ppm·m).

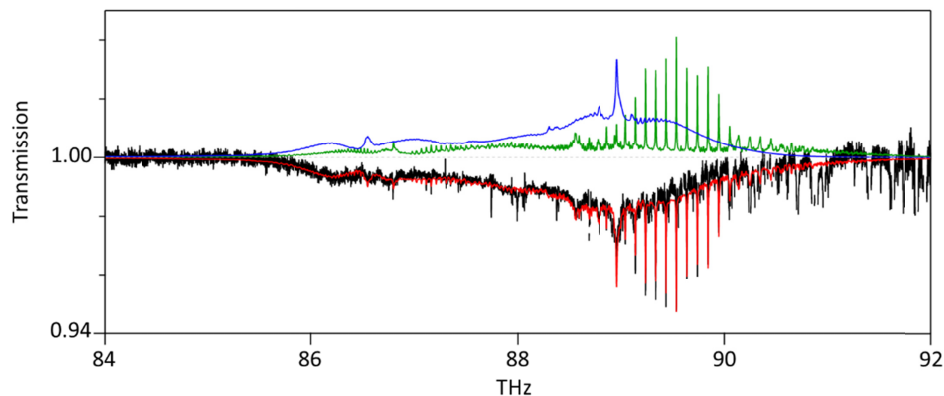


Fig. 7. Fit of ethane and propane. The black trace is the normalized DCS spectrum averaged over 1 hour (21:00 to 22:00, 3/7/2019) and smoothed to 2 GHz resolution with the cubic baseline polynomial, water and methane removed. The red line is the combined ethane and propane fit using the PNNL database, showing good agreement with the DCS measurement. Also shown are the individual spectra for ethane (green line, 14.2 ppm·m concentration) and propane (blue line, 18.8 ppm·m concentration).

The stability of the instrument makes continuous operation straight forward. Figure 8 shows 30 hours of continuous data over the outdoor path. The comb system ran independently for the entire period despite being in a room with an open window. Return power over the open path dropped occasionally with path alignment drifts and frost formation on the retroreflectors but with occasional manual alignment we were reliably able to retrieve gas concentrations over the

entire 30 hours. Heated retroreflectors and a tracking telescope would remove that requirement [19,20]. The broad bandwidth of the system allows simultaneous retrieval of ambient H₂O, CH₄, temperature, and ethane. N₂O was also retrieved although the signal was noisy due to its limited spectral signature in this region. The raw data set contains 12.3 million interferograms that are averaged to 180 points at ten-minute time resolution. To quantify the ethane sensitivity we calculate the standard deviation of retrieved ethane concentrations during a time window with low-to-zero background ethane levels around 3/7/2019, 15:45. This provides an upper limit to the sensitivity of 120 ppb·m·√minutes, representing 3-fold improvement over the previous work [28].

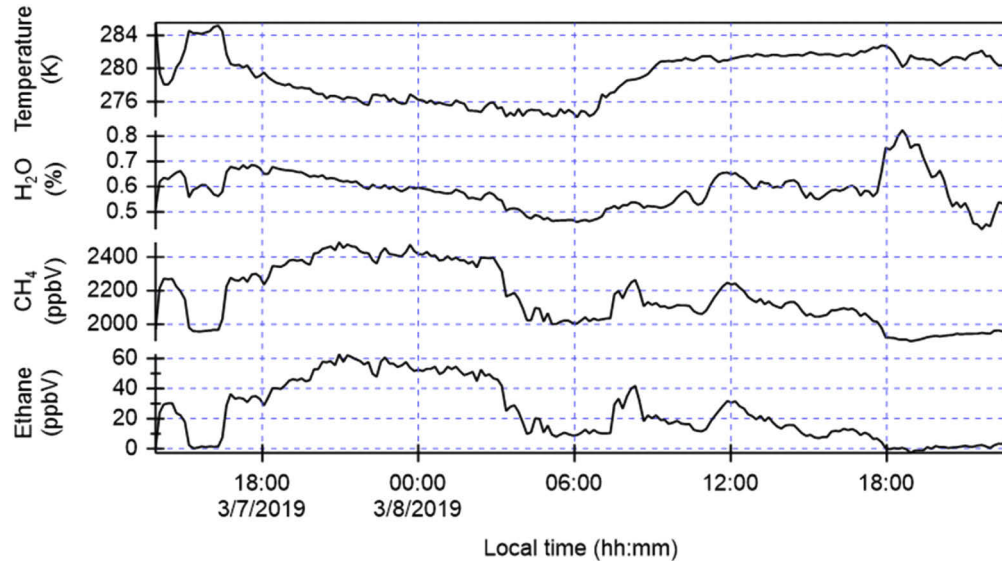


Fig. 8. Open-path gas retrievals over 30 hours of continuous operation.

The presented DCS system covers 25 THz with 125,000 resolved elements (200 MHz point sample spacing) and an average signal-to-noise ratio (SNR) of 120 for the signal channel, resulting in a figure of merit [62] of 2×10^6 . The figure of merit is limited, roughly equally, by the detector dynamic range and the laser relative intensity noise on the combs (-130 dBc/Hz). This compares favorably to both mid-IR and near-IR DCS systems [1]. However, it is worth noting that we have defined SNR as the standard deviation of the noise in a 1 THz window at the center of the spectrum. This definition provides a good measurement of the white noise but does not necessarily capture baseline distortions that can mask a broadly absorbing molecule such as propane. To estimate the sensitivity to broad absorbers, it is useful to calculate the SNR as the standard deviation over a much larger spectral window. Figure 9 shows the spectral signal channel SNR for a 1-minute measurement as well as the average 4-way normalized spectra's SNR as function of averaging time for different window sizes. As expected, the SNR increases with the square root of the averaging time. Moreover, the 6-THz window shows only a modest (2X) degradation in SNR compared to the narrow spectral window, indicating the effectiveness of the current background removal approach. For larger spectral windows, the calculated SNR is limited by spectral fluctuations arising from an imperfect fit to the many saturated water and methane absorption lines. An improved spectral model for water and methane lines in this region or use of a different masking function could reduce the impact of these saturated lines in the future. While we took 30 hours of data, the 512 minute (8.3 hour) stretch of data used in Fig. 9

represents the longest continuous stretch of time over which the return power over the path was fully optimal.

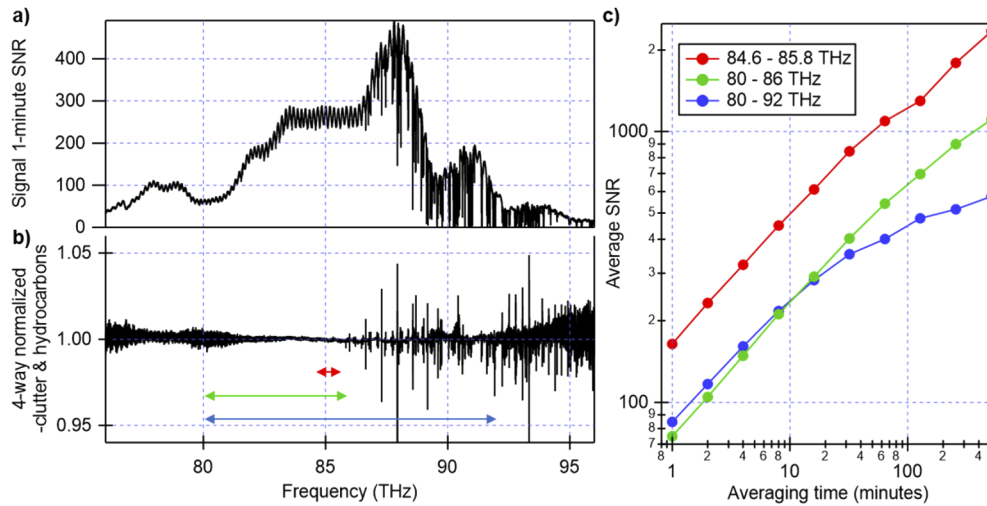


Fig. 9. Spectral SNR. a) spectral SNR for the raw signal channel averaged for 1 minute. b) spectral SNR for the 4-way normalized spectrum averaged for 512 minutes after H₂O and CH₄ removal. The different spectral windows of 1 THz, 6 THz and 12 THz widths used to calculate the different SNR values are indicated by arrows. c) Average SNR versus averaging time over a narrow 1 THz window, (red) a 6 THz window (green) and a 12 THz window (blue). The variations in SNR between spectral windows at short averaging times are due to differing average light power within the windows. The flattening of the 12 THz window SNR for longer averaging time is caused by spikes at spectral frequencies > 86 THz originating from imperfect removal of saturated water and methane lines in the spectral fit. Note that the SNR values in c) are lower than in a) due to the 4-way normalization.

5. Conclusion

We have demonstrated an open-path broadband mid-IR dual comb spectrometer operating in the 3.1- μm to 4.0- μm spectral region for field measurements of trace gases in the atmosphere. The design leverages highly stable, all-PM fiber near-IR frequency combs and DFG in high efficiency waveguide PPLN to greatly reduce system size, and complexity while increasing the robustness and stability. The improvements in both spectral coverage and baseline removal relative to [28] has increased the system's sensitivity to species with broad absorption features such as volatile organic compounds, which are emitted from an array of industrial processes. Given the improved robustness and detection capability demonstrated here, we expect we will be able to deploy the system at oil and gas extraction sites to measure and quantify emission levels for methane, ethane and an array of volatile organic chemicals.

Funding

Defense Advanced Research Projects Agency (SCOUT); Advanced Research Projects Agency - Energy (MONITOR).

Acknowledgments

Authors would like to acknowledge helpful comments from Nima Nader and Abijith Kowligy.

Disclosures

The authors declare no conflicts of interest. This is work of the U.S. Government and not subject to copyright.

References

1. I. Coddington, N. Newbury, and W. Swann, "Dual-comb spectroscopy," *Optica* **3**(4), 414–426 (2016).
2. F. Keilmann, C. Gohle, and R. Holzwarth, "Time-domain mid-infrared frequency-comb spectrometer," *Opt. Lett.* **29**(13), 1542–1544 (2004).
3. I. Coddington, W. C. Swann, and N. R. Newbury, "Coherent multiheterodyne spectroscopy using stabilized optical frequency combs," *Phys. Rev. Lett.* **100**(1), 013902 (2008).
4. P. Giaccari, J.-D. Deschênes, P. Saucier, J. Genest, and P. Tremblay, "Active Fourier-transform spectroscopy combining the direct RF beating of two fiber-based mode-locked lasers with a novel referencing method," *Opt. Express* **16**(6), 4347–4365 (2008).
5. J.-D. Deschênes, P. Giaccari, and J. Genest, "Optical referencing technique with CW lasers as intermediate oscillators for continuous full delay range frequency comb interferometry," *Opt. Express* **18**(22), 23358–23370 (2010).
6. J. Roy, J.-D. Deschênes, S. Potvin, and J. Genest, "Continuous real-time correction and averaging for frequency comb interferometry," *Opt. Express* **20**(20), 21932–21939 (2012).
7. S. Okubo, K. Iwakuni, H. Inaba, K. Hosaka, A. Onae, H. Sasada, and F.-L. Hong, "Ultra-broadband dual-comb spectroscopy across 1.0–1.9 μm ," *Appl. Phys. Express* **8**(8), 082402 (2015).
8. F. Zhu, A. Bicer, R. Askar, J. Bounds, A. A. Kolomenskii, V. Kelessides, M. Amani, and H. A. Schuessler, "Mid-infrared dual frequency comb spectroscopy based on fiber lasers for the detection of methane in ambient air," *Laser Phys. Lett.* **12**(9), 095701 (2015).
9. Y. Jin, S. M. Cristescu, F. J. M. Harren, and J. Mandon, "Femtosecond optical parametric oscillators toward real-time dual-comb spectroscopy," *Appl. Phys. B* **119**(1), 65–74 (2015).
10. O. Kara, Z. Zhang, T. Gardiner, and D. T. Reid, "Dual-comb mid-infrared spectroscopy with free-running oscillators and absolute optical calibration from a radio-frequency reference," *Opt. Express* **25**(14), 16072 (2017).
11. A. V. Muraviev, V. O. Smolski, Z. E. Loparo, and K. L. Vodopyanov, "Massively parallel sensing of trace molecules and their isotopologues with broadband subharmonic mid-infrared frequency combs," *Nat. Photonics* **12**(4), 209–214 (2018).
12. G. Ycas, F. R. Giorgetta, E. Baumann, I. Coddington, D. Herman, S. A. Diddams, and N. R. Newbury, "High-coherence mid-infrared dual-comb spectroscopy spanning 2.6 to 5.2 μm ," *Nat. Photonics* **12**(4), 202–208 (2018).
13. H. Timmers, A. Kowligy, A. Lind, F. C. Cruz, N. Nader, M. Silfies, G. Ycas, T. K. Allison, P. G. Schunemann, S. B. Papp, and S. A. Diddams, "Molecular fingerprinting with bright, broadband infrared frequency combs," *Optica* **5**(6), 727–732 (2018).
14. Z. Chen, T. W. Hänsch, and N. Picqué, "Mid-infrared feed-forward dual-comb spectroscopy," *Proc. Natl. Acad. Sci. U. S. A.* **116**(9), 3454–3459 (2019).
15. G.-W. Truong, E. M. Waxman, K. C. Cossel, E. Baumann, A. Klose, F. R. Giorgetta, W. C. Swann, N. R. Newbury, and I. Coddington, "Accurate frequency referencing for fieldable dual-comb spectroscopy," *Opt. Express* **24**(26), 30495–30504 (2016).
16. G. B. Rieker, F. R. Giorgetta, W. C. Swann, J. Kofler, A. M. Zolot, L. C. Sinclair, E. Baumann, C. Cromer, G. Petron, C. Sweeney, P. P. Tans, I. Coddington, and N. R. Newbury, "Frequency-comb-based remote sensing of greenhouse gases over kilometer air paths," *Optica* **1**(5), 290–298 (2014).
17. E. M. Waxman, K. C. Cossel, G.-W. Truong, F. R. Giorgetta, W. C. Swann, S. Coburn, R. J. Wright, G. B. Rieker, I. Coddington, and N. R. Newbury, "Intercomparison of open-path trace gas measurements with two dual-frequency-comb spectrometers," *Atmos. Meas. Tech.* **10**(9), 3295–3311 (2017).
18. E. M. Waxman, K. C. Cossel, F. Giorgetta, G.-W. Truong, W. C. Swann, I. Coddington, and N. R. Newbury, "Estimating vehicle carbon dioxide emissions from Boulder, Colorado, using horizontal path-integrated column measurements," *Atmos. Chem. Phys.* **19**(7), 4177–4192 (2019).
19. S. Coburn, C. B. Alden, R. Wright, K. Cossel, E. Baumann, G.-W. Truong, F. Giorgetta, C. Sweeney, N. R. Newbury, K. Prasad, I. Coddington, and G. B. Rieker, "Regional trace-gas source attribution using a field-deployed dual frequency comb spectrometer," *Optica* **5**(4), 320–327 (2018).
20. K. C. Cossel, E. M. Waxman, F. R. Giorgetta, M. Cermak, I. R. Coddington, D. Hesselius, S. Ruben, W. C. Swann, G.-W. Truong, G. B. Rieker, and N. R. Newbury, "Open-path dual-comb spectroscopy to an airborne retroreflector," *Optica* **4**(7), 724–728 (2017).
21. P. J. Schroeder, R. J. Wright, S. Coburn, B. Sodergren, K. C. Cossel, S. Droste, G. W. Truong, E. Baumann, F. R. Giorgetta, I. Coddington, N. R. Newbury, and G. B. Rieker, "Dual frequency comb laser absorption spectroscopy in a 16 MW gas turbine exhaust," *Proc. Combust. Inst.* **36**(3), 4565–4573 (2017).
22. A. D. Draper, R. K. Cole, A. S. Makowiecki, J. Mohr, A. Zdanowicz, A. Marchese, N. Hoghooghi, and G. B. Rieker, "Broadband dual-frequency comb spectroscopy in a rapid compression machine," *Opt. Express* **27**(8), 10814–10825 (2019).
23. A. Asahara, A. Nishiyama, S. Yoshida, K. Kondo, Y. Nakajima, and K. Minoshima, "Dual-comb spectroscopy for rapid characterization of complex optical properties of solids," *Opt. Lett.* **41**(21), 4971–4974 (2016).

24. A. Asahara and K. Minoshima, "Development of ultrafast time-resolved dual-comb spectroscopy," *APL Photonics* **2**(4), 041301 (2017).
25. A. Schliesser, N. Picqué, and T. W. Hänsch, "Mid-infrared frequency combs," *Nat. Photonics* **6**(7), 440–449 (2012).
26. M. Brehm, A. Schliesser, and F. Keilmann, "Spectroscopic near-field microscopy using frequency combs in the mid-infrared," *Opt. Express* **14**(23), 11222–11233 (2006).
27. A. Schliesser, M. Brehm, F. Keilmann, and D. van der Weide, "Frequency-comb infrared spectrometer for rapid, remote chemical sensing," *Opt. Express* **13**(22), 9029–9038 (2005).
28. G. Ycas, F. R. Giorgetta, K. C. Cossel, E. M. Waxman, E. Baumann, N. R. Newbury, and I. Coddington, "Mid-infrared dual-comb spectroscopy of volatile organic compounds across long open-air paths," *Optica*, *Optica* **6**(2), 165–168 (2019).
29. M. A. Abbas, Q. Pan, J. Mandon, S. M. Cristescu, F. J. M. Harren, and A. Khodabakhsh, "Time-resolved mid-infrared dual-comb spectroscopy," *Sci. Rep.* **9**(1), 1–9 (2019).
30. N. H. Pinkowski, Y. Ding, C. L. Strand, R. K. Hanson, R. Horvath, and M. Geiser, "Dual-comb spectroscopy for high-temperature reaction kinetics," *Meas. Sci. Technol.* **31**(5), 055501 (2020).
31. A. Foltynowicz, P. Masłowski, A. J. Fleisher, B. J. Bjork, and J. Ye, "Cavity-enhanced optical frequency comb spectroscopy in the mid-infrared application to trace detection of hydrogen peroxide," *Appl. Phys. B* **110**(2), 163–175 (2013).
32. A. J. Fleisher, B. J. Bjork, T. Q. Bui, K. C. Cossel, M. Okumura, and J. Ye, "Mid-Infrared Time-Resolved Frequency Comb Spectroscopy of Transient Free Radicals," *J. Phys. Chem. Lett.* **5**(13), 2241–2246 (2014).
33. J. L. Klocke, M. Mangold, P. Allmendinger, A. Hugi, M. Geiser, P. Jouy, J. Faist, and T. Kottke, "Single-Shot Sub-microsecond Mid-infrared Spectroscopy on Protein Reactions with Quantum Cascade Laser Frequency Combs," *Anal. Chem.* **90**(17), 10494–10500 (2018).
34. A. S. Kowligy, H. Timmers, A. J. Lind, U. Elu, F. C. Cruz, P. G. Schunemann, J. Biegert, and S. A. Diddams, "Infrared electric field sampled frequency comb spectroscopy," *Sci. Adv.* **5**(6), eaaw8794 (2019).
35. J. Faist, G. Villares, G. Scalari, M. Rösch, C. Bonzon, A. Hugi, and M. Beck, "Quantum Cascade Laser Frequency Combs," *Nanophotonics* **5**(2), 272–291 (2016).
36. G. Villares, A. Hugi, S. Blaser, and J. Faist, "Dual-comb spectroscopy based on quantum-cascade-laser frequency combs," *Nat. Commun.* **5**(1), 5192 (2014).
37. L. Consolino, S. Bartalini, and P. De Natale, "Terahertz Frequency Metrology for Spectroscopic Applications: a Review," *J. Infrared Milli. Terahz. Waves* **38**(11), 1289–1315 (2017).
38. L. A. Sterczewski, L. A. Sterczewski, L. A. Sterczewski, J. Westberg, and G. Wysocki, "Computational coherent averaging for free-running dual-comb spectroscopy," *Opt. Express* **27**(17), 23875–23893 (2019).
39. J. Westberg, L. A. Sterczewski, and G. Wysocki, "Mid-infrared multiheterodyne spectroscopy with phase-locked quantum cascade lasers," *Appl. Phys. Lett.* **110**(14), 141108 (2017).
40. P. Jouy, J. M. Wolf, Y. Bidaux, P. Allmendinger, M. Mangold, M. Beck, and J. Faist, "Dual comb operation of $\lambda \sim 8.2 \mu\text{m}$ quantum cascade laser frequency comb with 1 W optical power," *Appl. Phys. Lett.* **111**(14), 141102 (2017).
41. D. Burghoff, Y. Yang, and Q. Hu, "Computational multiheterodyne spectroscopy," *Sci. Adv.* **2**(11), e1601227 (2016).
42. Y. Yang, D. Burghoff, D. J. Hayton, J.-R. Gao, J. L. Reno, and Q. Hu, "Terahertz multiheterodyne spectroscopy using laser frequency combs," *Optica* **3**(5), 499–502 (2016).
43. L. A. Sterczewski, J. Westberg, M. Bagheri, C. Frez, I. Vurgaftman, C. L. Canedy, W. W. Bewley, C. D. Merritt, C. S. Kim, M. Kim, J. R. Meyer, and G. Wysocki, "Mid-infrared dual-comb spectroscopy with interband cascade lasers," *Opt. Lett.* **44**(8), 2113–2116 (2019).
44. M. Yan, P.-L. Luo, K. Iwakuni, G. Millot, T. W. Hänsch, and N. Picqué, "Mid-infrared dual-comb spectroscopy with electro-optic modulators," *Light: Sci. Appl.* **6**(10), e17076 (2017).
45. B. Jerez, P. Martín-Mateos, F. Walla, C. de Dios, and P. Acedo, "Flexible Electro-Optic, Single-Crystal Difference Frequency Generation Architecture for Ultrafast Mid-Infrared Dual-Comb Spectroscopy," *ACS Photonics* **5**(6), 2348–2353 (2018).
46. E. Baumann, F. R. Giorgetta, W. C. Swann, A. M. Zolot, I. Coddington, and N. R. Newbury, "Spectroscopy of the methane ν_3 band with an accurate midinfrared coherent dual-comb spectrometer," *Phys. Rev. A* **84**(6), 062513 (2011).
47. F. C. Cruz, D. L. Maser, T. Johnson, G. Ycas, A. Klose, F. R. Giorgetta, I. Coddington, and S. A. Diddams, "Mid-infrared optical frequency combs based on difference frequency generation for molecular spectroscopy," *Opt. Express* **23**(20), 26814 (2015).
48. I. Galli, F. Cappelli, P. Cancio, G. Giusfredi, D. Mazzotti, S. Bartalini, and P. D. Natale, "High-coherence mid-infrared frequency comb," *Opt. Express* **21**(23), 28877–28885 (2013).
49. Y. Jin, S. M. Cristescu, F. J. M. Harren, and J. Mandon, "Two-crystal mid-infrared optical parametric oscillator for absorption and dispersion dual-comb spectroscopy," *Opt. Lett.* **39**(11), 3270–3273 (2014).
50. Z. Zhang, T. Gardiner, and D. T. Reid, "Mid-infrared dual-comb spectroscopy with an optical parametric oscillator," *Opt. Lett.* **38**(16), 3148–3150 (2013).
51. F. Adler, P. Masłowski, A. Foltynowicz, K. C. Cossel, T. C. Briles, I. Hartl, and J. Ye, "Mid-infrared Fourier transform spectroscopy with a broadband frequency comb," *Opt. Express* **18**(21), 21861 (2010).

52. A. Khodabakhsh, V. Ramaiah-Badarla, L. Rutkowski, A. C. Johansson, K. F. Lee, J. Jiang, C. Mohr, M. E. Fermann, and A. Foltynowicz, "Fourier transform and Vernier spectroscopy using an optical frequency comb at 3–5.4 μm ," *Opt. Lett.* **41**(11), 2541–2544 (2016).
53. L. C. Sinclair, J.-D. Deschênes, L. Sonderhouse, W. C. Swann, I. H. Khader, E. Baumann, N. R. Newbury, and I. Coddington, "Invited Article: A compact optically coherent fiber frequency comb," *Rev. Sci. Instrum.* **86**(8), 081301 (2015).
54. J. Moses, H. Suchowski, and F. X. Kärtner, "Fully efficient adiabatic frequency conversion of broadband Ti:sapphire oscillator pulses," *Opt. Lett.* **37**(9), 1589 (2012).
55. H. Suchowski, V. Prabhudesai, D. Oron, A. Arie, and Y. Silberberg, "Robust adiabatic sum frequency conversion," *Opt. Express* **17**(15), 12731 (2009).
56. Z. Zhu, K. Ni, Q. Zhou, and G. Wu, "Digital correction method for realizing a phase-stable dual-comb interferometer," *Opt. Express* **26**(13), 16813–16823 (2018).
57. T. Ideguchi, A. Poisson, G. Guelachvili, N. Picqué, and T. W. Hänsch, "Adaptive real-time dual-comb spectroscopy," *Nat. Commun.* **5**(1), 3375 (2014).
58. M. Cassinero, A. Gambetta, N. Coluccelli, P. Laporta, and G. Galzerano, "Absolute dual-comb spectroscopy at 1.55 μm by free-running Er:fiber lasers," *Appl. Phys. Lett.* **104**(23), 231102 (2014).
59. C. E. Shannon, "Communication in the Presence of Noise," *Proc. IRE* **37**(1), 10–21 (1949).
60. I. E. Gordon, L. S. Rothman, C. Hill, R. V. Kochanov, Y. Tan, P. F. Bernath, M. Birk, V. Boudon, A. Campargue, K. V. Chance, B. J. Drouin, J.-M. Flaud, R. R. Gamache, J. T. Hodges, D. Jacquemart, V. I. Perevalov, A. Perrin, K. P. Shine, M.-A. H. Smith, J. Tennyson, G. C. Toon, H. Tran, V. G. Tyuterev, A. Barbe, A. G. Császár, V. M. Devi, T. Furtenbacher, J. J. Harrison, J.-M. Hartmann, A. Jolly, T. J. Johnson, T. Karman, I. Kleiner, A. A. Kyuberis, J. Loos, O. M. Lyulin, S. T. Massie, S. N. Mikhailenko, N. Moazzen-Ahmadi, H. S. P. Müller, O. V. Naumenko, A. V. Nikitin, O. L. Polyansky, M. Rey, M. Rotger, S. W. Sharpe, K. Sung, E. Starikova, S. A. Tashkun, J. V. Auwera, G. Wagner, J. Wilzewski, P. Wcisło, S. Yu, and E. J. Zak, "The HITRAN2016 molecular spectroscopic database," *J. Quant. Spectrosc. Radiat. Transfer* **203**, 3–69 (2017).
61. S. W. Sharpe, T. J. Johnson, R. L. Sams, P. M. Chu, G. C. Rhoderick, and P. A. Johnson, "Gas-Phase Databases for Quantitative Infrared Spectroscopy," *Appl. Spectrosc.* **58**(12), 1452–1461 (2004).
62. N. R. Newbury, I. Coddington, and W. C. Swann, "Sensitivity of coherent dual-comb spectroscopy," *Opt. Express* **18**(8), 7929–7945 (2010).